J. Fluid Mech. (1990), *vol.* 213, *pp.* 127–148
Printed in Great Britain

The dynamics of a localized surfactant on a thin film

By DONALD P. GAVER, III† AND JAMES B. GROTBERG

Biomedical Engineering Department, Northwestern University, Evanston, IL 60208, USA *and*
Department of Anesthesia, Northwestern University Medical School, 303 East Chicago Avenue,
Chicago, IL 60611, USA

(Received 1 March 1989 and in revised form 7 August 1989)

We investigate the flow induced by a localized insoluble surfactant on a thin film. This problem is intended to model the behaviour of the lung's thin-film lining after an aerosol droplet lands on its surface. The surfactant-induced surface-tension gradients drive convection (Marangoni convection) within the film, disrupting the film surface and causing the surfactant to spread. The surfactant may also spread on the film's surface by surface diffusion without inducing convection. Gravity provides a restoring force that decreases film disturbances.

Lubrication theory is employed to derive equations that describe the evolution of the film thickness and surfactant concentration. A nonlinear surface-tension equation of state describes the relationship between the surfactant concentration and the surface tension. Solutions of the evolution equations are found numerically using the method of lines and analytically under limiting cases of small and large surface diffusivity. The results elucidate the behaviour of the thin-film/surfactant system.

We find that surface-tension-induced convection creates film disturbances that increase the film thickness near the surfactant's leading edge, and thins the film in the central region. Surface diffusion causes more rapid spreading of the surfactant, and decreases the film disturbances. Gravity decreases the film disturbances by creating bi-directional flow in the form of a ring vortex. This behaviour may have implications for the delivery of medications or toxins by aerosol inhalation.

1. Introduction

The interiors of pulmonary airways and alveoli provide a large surface area, of the order of 100 m^2, for the exchange of respiratory gases. This surface is coated with a thin liquid lining which serves as a barrier between the air and tissues not only for gas exchange, but also for any airborne particle or aerosol. When an aerosol droplet is inhaled, the transport of its contained materials ultimately depends on the droplet interaction with this liquid lining. Common medical applications include the delivery of aerosols for bronchodilator therapy to treat asthmatics. More recently antibiotics have been delivered in this manner, particularly for pulmonary infections such as are encountered in Acquired Immune Deficiency Syndrome (AIDS) (Conte, Hollander & Golden 1987). Not only can medications be delivered, but also environmental pollutants can 'piggyback' onto normally innocuous aerosol droplets and reach sensitive regions of the lung (Goetz 1961).

A relatively common disease in premature neonates is hyaline membrane disease,

---

† Present address: Department of Biomedical Engineering, Tulane University, New Orleans, LA 70118-5674, USA.

whose major feature is an abnormally high surface tension of the lung's liquid lining. This results from the immature lung's inability to produce surfactants. One treatment for this disease is the delivery of exogenous surfactants into the respiratory tract (Enhorning *et al.* 1985; Merritt *et al.* 1986). Although a number of delivery methods are used, aerosol delivery has been attempted (Zelter *et al.* 1988), and may optimally deliver the surfactant to the distal bronchi. The dynamical interaction of the aerosol spray and the liquid lining are not known, though the treatment can be effective.

Previous investigations of inhaled aerosols have focused on the deposition sites as a function of the aerosol's aerodynamic radius (Schreck 1982). While the distribution of the aerosols within the bronchial tree provides some information concerning the delivery of substances, it gives no insight into the interaction of the aerosol droplet with the thin-film lining the lung. For instance, surface-active constituents could cause the aerosol to spread and induce motion within the thin film. Depending upon the spreading characteristics: (i) the rate of transport of a diffusible solute to the parenchyma may be modified from that of pure diffusion; (ii) the thickness and physical characteristics of the lining may be changed; (iii) the clearance of the droplet from the lung might be enhanced or retarded; (iv) overall properties of the lung such as compliance and its frequency dependence could change.

To investigate the 'working end' of the aerosol delivery system, the aerosol will be modelled by the presence of a surface active contaminant on a thin film, which is intended to describe the situation that exists shortly after aerosol deposition onto the lung's liquid lining. A fluid mechanical investigation of this situation should provide useful information towards understanding the droplet/lung-lining interaction. As a first step in understanding the transport of contaminant through the lung's liquid lining, we hope to elucidate the film's response to the deposition of an insoluble surface-active material.

Existing analyses of contaminant spreading on deep liquid layers (DiPietro, Huh & Cox 1978; DiPietro & Cox 1980; Foda & Cox 1980; Dagan 1984) are not suitable for application to the lung's thin liquid lining, principally because the substrate flow is high Reynolds number, which leads to boundary-layer formation beneath the contaminant, while in the thin-film case a low-Reynolds-number viscous flow exists. For this reason, the resistive force due to viscous drag of the thin-film substrate will be larger than that of the deep-liquid case, and the spreading rates should be slower. While these studies are not directly applicable for analysis in the lung, they provide a comprehensive overview of the interfacial mechanics associated with the spreading-droplet problem. A review of these analyses is provided by Borgas & Grotberg (1988).

Studies of surface tension driven flows on thin films have been published by Yih (1968, 1969), Levich (1962), Joos & Pintens (1977), Adler & Sowerby (1970), Ahmad & Hansen (1972), Hussain, Fatima & Ahmad (1975), Dagan (1984) and Borgas & Grotberg (1988). All of these theories, with the exception of Adler & Sowerby (1970), investigate the problem of a moving planar front. Adler & Sowerby used the full three-dimensional geometry, but investigated only flows induced by known variations of surface tension; they did not relate these gradients to a surfactant. Yih (1968) studied the flow within a constraining channel, and the other studies listed above involved unconstrained spreading. In general, these studies assume monolayer dynamics, and use steady forms of the governing equations to investigate unsteady phenomena, which at best leads to results that are valid in a 'quasi-steady' limit.

Within this paper, we present our investigation of the time-dependent flows created by the spreading of a surface-active contaminant on a thin film. In the analysis of this problem the dimensional governing equations allowing surface-tension-gradient-driven flows, gravitational forcing and surface diffusivity of the surfactant are derived. Here the interfacial surface tension depends directly upon the surface concentration of the surfactant. The initial surface-tension distribution drives the fluid flow within the initially flat thin film, and thus determines the dynamics of the full mechanical system. This system consists of the film thickness, radial and vertical velocity fields and a time-dependent surfactant distribution.

We formulate this problem and introduce the governing equations in §2. We derive evolution equations that describe the film thickness and surfactant concentration profiles in §3. These equations are numerically integrated, and the results are presented in §4. Sections 5 and 6 present our analyses of large and small Péclet-number flows, respectively, and in §7 we discuss the cumulative results of our numerical and analytical solutions. Finally, the conclusions are presented in §8, where we compare our results to those of other investigators and relate our findings to the delivery of medication by aerosol inhalation.

2. Problem formulation

A thin film of a Newtonian fluid with viscosity, μ, and density, ρ, is bounded below by a horizontal rigid wall at $z = 0$ and above by the interface position $z = H(r, t)$. We model axisymmetric spreading in cylindrical coordinates (r, θ, z) with respective fluid velocity components $(v_r, 0, v_z)$ and pressure, P. The surface tension, $\sigma(\Gamma)$, is a function of the surface concentration of insoluble surfactant, $\Gamma(r, t)$. The problem is formulated in dimensionless variables whose relation to the dimensional variables (denoted by *) is given by

$$\left.\begin{aligned} r^* = R_0 r, \quad z^* = H_0 z, \quad \sigma^* = \sigma_m + S\sigma, \\ v_r^* = U v_r = \frac{SH_0}{\mu R_0} v_r, \quad v_z^* = \frac{H_0 U}{R_0} v_z, \quad t^* = \frac{\mu R_0^2}{SH_0} t, \\ \Gamma^* = \Gamma_m \Gamma, \quad P^* = \frac{S}{H_0} P, \end{aligned}\right\} \tag{2.1}$$

where R_0 is the initial radius of the spreading surfactant, H_0 is the initial uniform thickness of the thin film, U is found by scaling the tangential-stress condition for a flat interface and the timescale is appropriate for convective events. σ_m is the surface tension of the interface when $\Gamma^* = \Gamma_m$, the micelle, or saturation monolayer surfactant concentration. We define the spreading parameter, $S = \sigma_0 - \sigma_m$ where σ_0 is the surface tension of the surfactant-free interface ($\Gamma = 0$).

By defining the ratio of lengthscales as $\epsilon = H_0/R_0$, the lubrication approximation is achieved by taking the limit $\epsilon \to 0$ in the governing equations, described below. Using the scales defined above, the r and z components of the Navier–Stokes equations, respectively, simplify to

$$-\frac{\partial P}{\partial r} + \frac{\partial^2 v_r}{\partial z^2} = O(\epsilon^2, \epsilon^2 Re), \quad -\frac{\partial P}{\partial z} - G = O(\epsilon^2), \tag{2.2a, b}$$

where $Re = UR_0/\nu$ is the Reynolds number and $G = \rho H_0^2 g/S$ is the ratio of gravity to surface-tension gradient (Marangoni) forces. The product $\epsilon^2 Re$ is assumed to be negligible for the thin-film flow.

The scaled continuity equation is given by

$$\frac{\partial v_z}{\partial z} = -\frac{1}{r}\frac{\partial}{\partial r}[r v_r], \tag{2.3}$$

and the boundary conditions of no-slip and no-penetration at the wall are

$$v_r = v_z = 0 \quad \text{on } z = 0. \tag{2.4}$$

In this model the surfactant is allowed to diffuse along the interface with constant diffusivity, D_s, or be convected along the surface of the thin film. The dimensional conservation equation for this surfactant is

$$\frac{\partial \Gamma^*}{\partial t^*} = D_s \nabla_s^{*2} \Gamma^* - \mathrm{div}_s(\boldsymbol{u}_s^* \Gamma^*) + \kappa^* \Gamma^* V^*. \tag{2.5}$$

Sequentially, left to right, the terms on the right-hand side of this equation represent the transport of surfactant by surface diffusion, the transport by convection, and an effective source–sink term that represents surface-concentration variations due to interfacial deformation. In this equation, $\boldsymbol{u}_s^*$ is the surface tangential velocity vector, V^* is the surface velocity normal to the interface, div_s is the surface divergence operator, ∇_s^* is the surface Laplacian operator, and κ^* is the interfacial curvature. The dimensionless version of this equation, omitting terms of $O(\epsilon)$, is given by,

$$\frac{\partial \Gamma}{\partial t} = \frac{1}{Pe}\left\{\frac{\partial^2 \Gamma}{\partial r^2} + \frac{1}{r}\frac{\partial \Gamma}{\partial r}\right\} - \frac{1}{r}\frac{\partial}{\partial r}[r v_r \Gamma] + O(\epsilon) \quad \text{at } z = H, \tag{2.6}$$

where $Pe = UR_0/D_s = SH_0/\mu D_s$ is the surface Péclet number, the ratio of convection to surface diffusion for the surfactant.

The non-dimensional form of the kinematic boundary condition is

$$\frac{\partial H}{\partial t} = v_z - v_r \frac{\partial H}{\partial r} \quad \text{on } z = H, \tag{2.7}$$

while the normal-stress jump condition at the interface takes the form

$$-P = \epsilon^2 \beta \left[\frac{\partial^2 H}{\partial r^2} + \frac{1}{r}\frac{\partial H}{\partial r}\right] + O(\epsilon^2) \quad \text{on } z = H, \tag{2.8}$$

where $\beta = \sigma_m / S$ is the ratio of the minimum surface tension to the spreading parameter S, and $\epsilon^2 \beta$ represents the ratio of capillary driving forces to the driving forces due to surface-tension gradients. The tangential-stress condition is the balance between viscous shear and the surface tension gradient

$$\frac{\partial v_r}{\partial z} = \frac{\partial \sigma}{\partial r} + O(\epsilon) \quad \text{on } z = H, \tag{2.9}$$

and provides the forcing for the convection.

Finally, the surface-tension equation of state takes the same form used by Sheludko (1967) and Borgas & Grotberg (1988)

$$\sigma(\Gamma) = (\beta + 1)\{1 + \Theta(\beta)\Gamma\}^{-3} - \beta, \tag{2.10}$$

where $\Theta(\beta) = ((\beta+1)/\beta)^{\frac{1}{3}} - 1$.

3. The evolution equations

The leading-order balance of the normal-stress equation (2.8) and z-component of the Navier–Stokes equation (2.2b) are used to calculate the leading-order pressure field,

$$P(r,z,t) = G[H(r,t)-z]-\epsilon^2\beta\left[\frac{\partial^2 H}{\partial r^2}+\frac{1}{r}\frac{\partial H}{\partial r}\right]. \tag{3.1}$$

This pressure field is due to both gravitational and capillary forces. Terms of order $\epsilon^2\sigma$ have been neglected, since the magnitude of σ is at most unity. Terms of $O(\epsilon^2\beta)$ are retained since some systems may exist in which this is $O(1)$. The retention of these terms preserves capillarity as a driving force. Additionally, terms of $O(G)$ allow gravitational forcing.

The reduced form of the radial non-dimensional Navier–Stokes equation (2.2), leading-order tangential-stress balance from (2.9) and the no-slip condition at the bottom wall (2.4a), are then used to determine the radial velocity field,

$$v_r(r,z,t) = \frac{\partial P}{\partial r}[\tfrac{1}{2}z^2-zH]+\frac{\partial \sigma}{\partial \Gamma}\frac{\partial \Gamma}{\partial r}z. \tag{3.2}$$

Continuity (2.3) and the no-penetration condition (2.4) are used to determine v_z,

$$v_z = -\frac{1}{r}\frac{\partial}{\partial r}\left\{r\left[\frac{\partial P}{\partial r}(\tfrac{1}{2}z^2H-\tfrac{1}{6}z^3)-\tfrac{1}{2}z^2\frac{\partial \sigma}{\partial \Gamma}\frac{\partial \Gamma}{\partial r}\right]\right\}. \tag{3.3}$$

The surface-tension equation of state (2.10) is then substituted into the velocity field, equations (3.2) and (3.3). This transforms the dependency of the velocity components to functions of surfactant concentration and film thickness. These equations are then substituted into the kinematic boundary condition, equation (2.7), and the reduced form of the dimensionless conservation of surfactant equation (2.6) to develop the evolution equations for film thickness and surfactant concentrations.

The resulting evolution equations are:

$$\frac{\partial H}{\partial t} = \frac{1}{r}\frac{\partial}{\partial r}\left\{r\left[\frac{1}{3}\frac{\partial P}{\partial r}H^3-\tfrac{1}{2}H^2\frac{\partial \sigma}{\partial \Gamma}\frac{\partial \Gamma}{\partial r}\right]\right\}, \tag{3.4}$$

and

$$\frac{\partial \Gamma}{\partial t} = \frac{1}{r}\frac{\partial}{\partial r}\left\{r\left[\left(\frac{1}{Pe}-\Gamma H\frac{\partial \sigma}{\partial \Gamma}\right)\frac{\partial \Gamma}{\partial r}+\frac{\partial P}{\partial r}\tfrac{1}{2}\Gamma H^2\right]\right\}. \tag{3.5}$$

Since, from equation (3.1), $\partial P/\partial r$ has third-order spatial derivatives, the evolution equations are fourth-order partial differential equations. We shall neglect capillarity ($\epsilon^2\beta \rightarrow 0$) so that the evolution equations (3.4) and (3.5) are reduced to second order in space.

Initial conditions must be introduced if the evolution equations are to be solved. The distribution of surfactant after the initial deposition of an aerosol on a thin film is not known, so we assume a distribution that might have the correct form. Qualitatively, this surfactant distribution resembles a smoothed disk of surfactant. Additionally, the film is assumed to be flat initially. Specifically, these initial conditions are:

$$\Gamma(r,0) = \begin{cases} \Gamma_{\max} & (\mathrm{r} \leqslant RI), \\ \Gamma_{\max}\left\{0.5\cos\left[\dfrac{\pi(r-RI)}{(1-RI)}\right]+0.5\right\} & (RI < r \leqslant 1.0), \\ 0 & (r > 1.0), \end{cases} \tag{3.6a}$$

$$H(r,0) = 1 \quad (r \geqslant 0). \tag{3.6b}$$

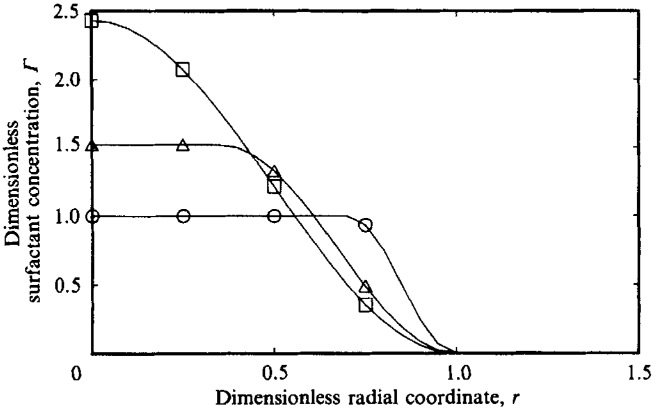

FIGURE 1. Initial surfactant concentration distribution profiles. □, $RI = 0$; △, $RI = 0.35$; ○, $RI = 0.7$. $V_S = 2.29$

This form of $\Gamma(r, 0)$ places the initial non-zero surface-concentration gradients from $RI < r < 1$, where RI is an adjustable parameter. Γ_{max} is used to determine the volume of surfactant after RI has been selected. Figure 1 shows initial surfactant concentration profiles for values of $RI = 0$, 0.35 and 0.7 with the volume of surfactant fixed at

$$V_S = 2\pi \int_0^1 r\Gamma(r, 0)\,\mathrm{d}r = 2.29.$$

Finally, the boundary conditions for these second-order equations are:

$$\frac{\partial \Gamma}{\partial r} = \frac{\partial H}{\partial r} = 0 \quad \text{on } r = 0, \qquad (3.7a, b)$$

and

$$\Gamma = 0, H = 1 \quad \text{as } r \to \infty. \qquad (3.7c, d)$$

To develop insight into the streamline patterns associated with this problem, the associated stream function was calculated. In this geometry, the stream function, ψ, is defined as:

$$\frac{\partial \psi}{\partial z} = -rv_r, \quad \frac{\partial \psi}{\partial r} = v_z, \qquad (3.8a, b)$$

and the bottom wall is defined as a streamline, $\psi = 0$ on $z = 0$. Here the stream function is scaled as

$$\psi^* = H_0 R_0 U \psi. \qquad (3.9)$$

The stream function is thus found to be

$$\psi = -r\left\{\frac{\partial P}{\partial r}\left[\tfrac{1}{6}z^3 - \tfrac{1}{2}z^2 H\right] + \tfrac{1}{2}z^2 \frac{\partial \sigma}{\partial \Gamma}\frac{\partial \Gamma}{\partial r}\right\}. \qquad (3.10)$$

In this equation, ψ depends upon values of H and Γ, which must first be obtained by the integration of equations (3.4) and (3.5).

4. Results

Solutions of the coupled, nonlinear evolution equations (3.4) and (3.5) with initial conditions provided by equation (3.6a, b) and boundary conditions listed in equations (3.7a–d) were found for a number of different values of time and dimensionless parameter groupings by the numerical Method of Lines.

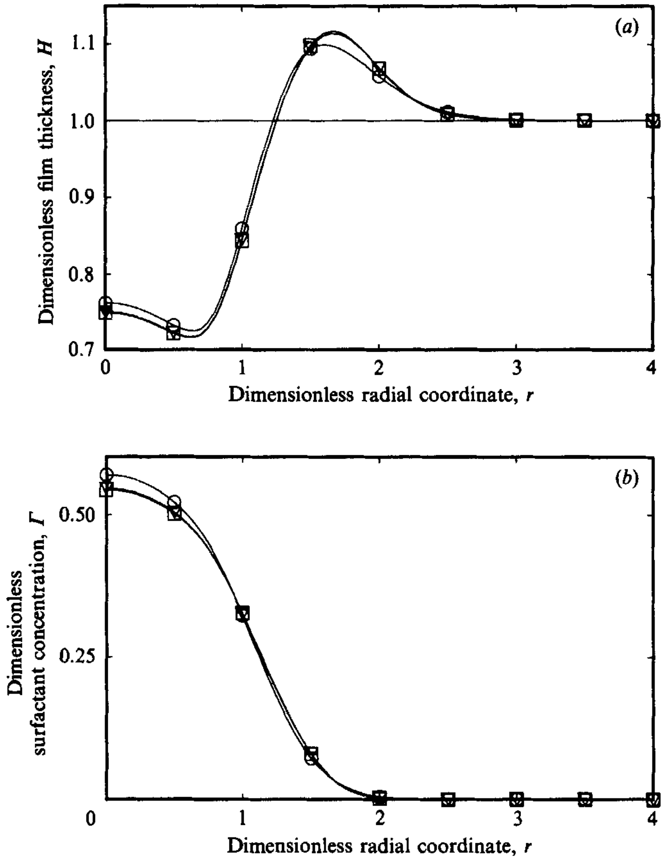

FIGURE 2. Convergence test for the method of lines. ○, tol = 0.1 ; ▽, tol = 0.01 ; □, tol = 0.001. $G = 1$, $Pe = 10$, $\beta = 5$, $RI = 0.7$, $\Gamma_{\max} = 1.0$ and $t = 0.5$.

To determine the convergence behaviour of the solution of the evolution equations subject to the imposed initial and boundary conditions, the tolerance of the method was selected as 0.1, 0.01 and 0.001. Our method was adaptive, modifying the temporal step size to satisfy the imposed tolerance criterion. Figure 2 displays the results of this calculation at $t = 0.5$, where the parameters chosen are $G = 1.0$, $Pe = 10$, $\beta = 5$, $RI = 0.7$ and $\Gamma_{\max} = 1$. These values represent our basic parameter set, and were selected purely for illustrative purposes. Such a parameter grouping may not occur during an actual experiment, however this grouping allows all mechanisms to be represented. These figures show that a tolerance of 0.01 is sufficient for the calculation of consistent results for this parameter grouping. To ensure consistency, the tolerance was chosen as 0.001 for all remaining calculations.

Figure 3 displays streamlines that characterize the flow patterns observed for all cases in which G is non-zero. Here the values of the dimensionless parameters are identical to those listed above, and these figures show the streamlines at three instants of time. Figure 3(*a*) shows the film deformation after only a very short amount of time ($t = 0.25$) with streamlines indicating velocities that are uniformly radially outward. As time progresses ($t = 0.75$) a vortex evolves at the wall in the region of radially increasing film thickness, $\partial H/\partial r > 0$, as can be seen in figure 3(*b*). This vortex then engulfs the film behind the moving front, as shown in figure 3(*c*).

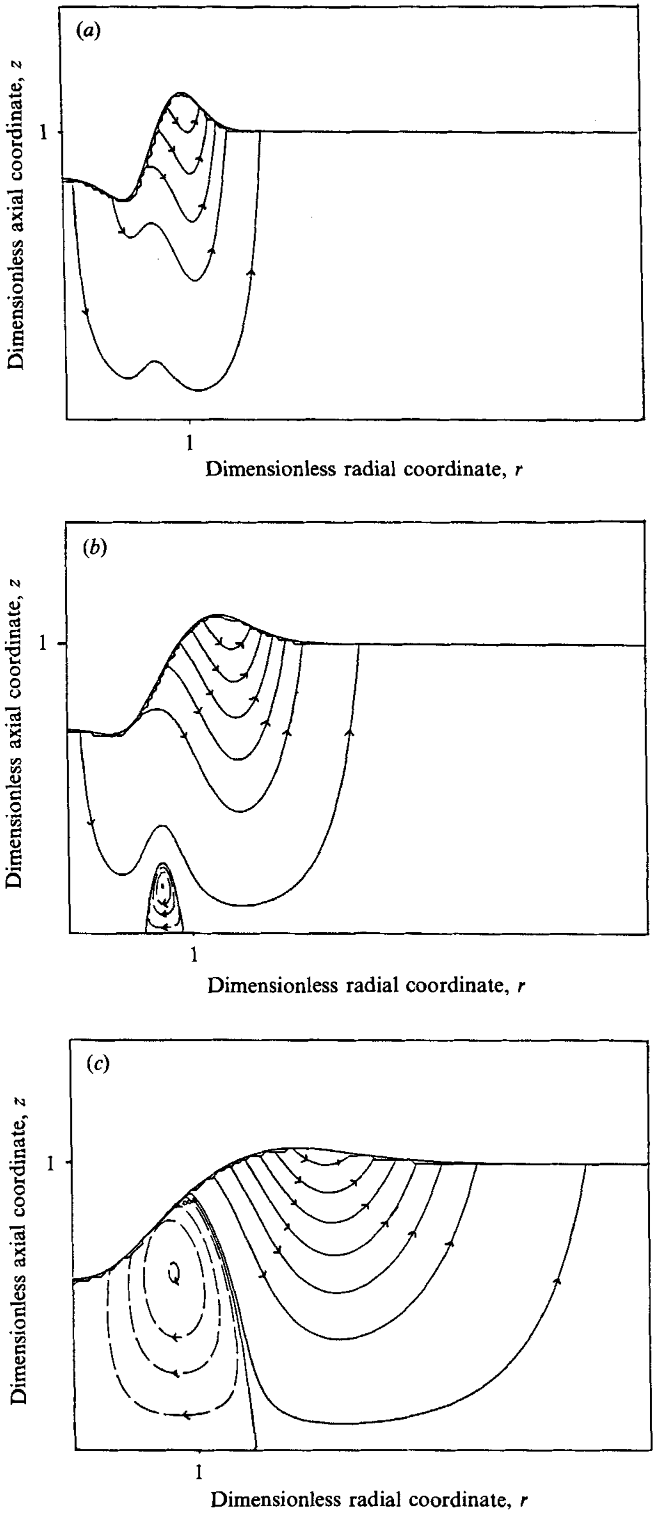

Figure 3. Streamlines representative of the Eulerian velocity field. (*a*) $t = 0.25$; (*b*) $t = 0.75$; (*c*) $t = 3.0$. $Pe = 10.0$, $G = 1.0$, $\beta = 5$, $RI = 0.7$ and $\Gamma_{\max} = 1.0$.

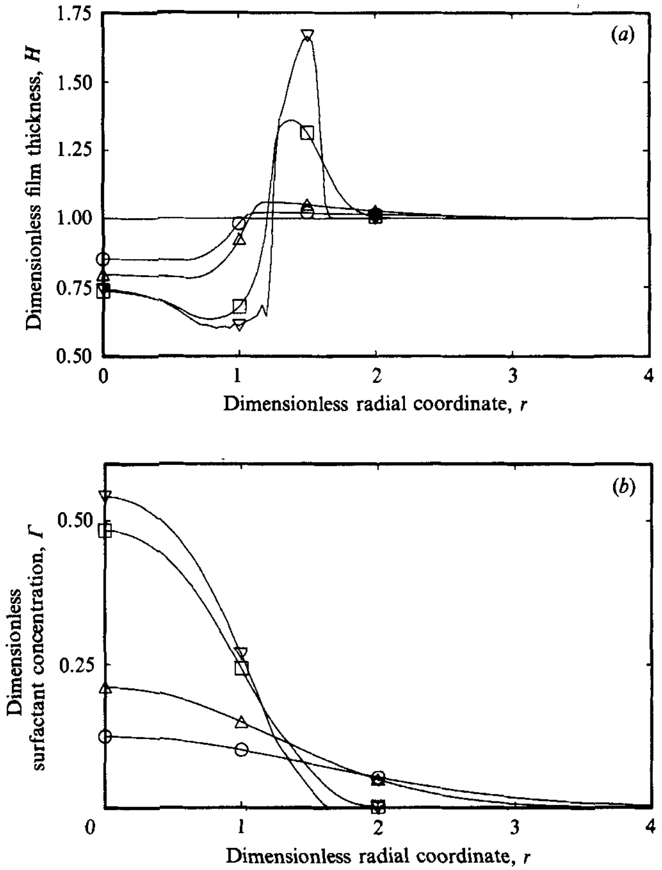

FIGURE 4. Film thickness and surfactant concentration profiles for ○, $Pe = 0.5$; △, $Pe = 1.0$; □, $Pe = 10.0$; ▽, $Pe = 100.0$. $G = 0$, $\beta = 5.0$, $RI = 0.7$, $\Gamma_{max} = 1.0$ and $t = 0.5$.

As the magnitudes of the dimensionless parameters are varied with $G > 0$, this basic sequence of events remains the same.

The influence of the Péclet number, Pe, is demonstrated by figure 4. Here the gravitational forcing is absent ($G = 0$), and Pe equals 0.5, 1.0, 10.0 and 100.0, so that the full range of diffusive and convective spreading phenomena can be compared. If these profiles are to represent behaviour that exists with film properties and t^* fixed, an increase in $Pe = SH_0/\mu D_s$ must be accomplished by a decrease in D_s. If interpreted in this manner, figure 4(*b*) indicates that an increase of Pe leads to reduced surfactant spreading rates, and a greater retention of the surfactant concentration distribution's initially steep gradients. Furthermore, figure 4(*a*) demonstrates that increasing the Péclet number leads to larger film disturbances, with a large leading-edge slope, and a thinning of the film in the region directly preceding the front.

The gravitational parameter G, influences the behaviour of the film and surfactant as shown by figure 5(*a*, *b*). Here Γ and H profiles are investigated for values of G equal to 0.1, 1 and 10. Figure 5 demonstrates that an increase in G leads to diminished film-thickness gradients, an increase of surfactant concentration near the centre of the droplet, and a decrease of the droplet's radius. As β is varied with other parameters fixed, the relationship between surfactant concentration and surface tension is modified, as indicated by the surface tension equation of state (2.10).

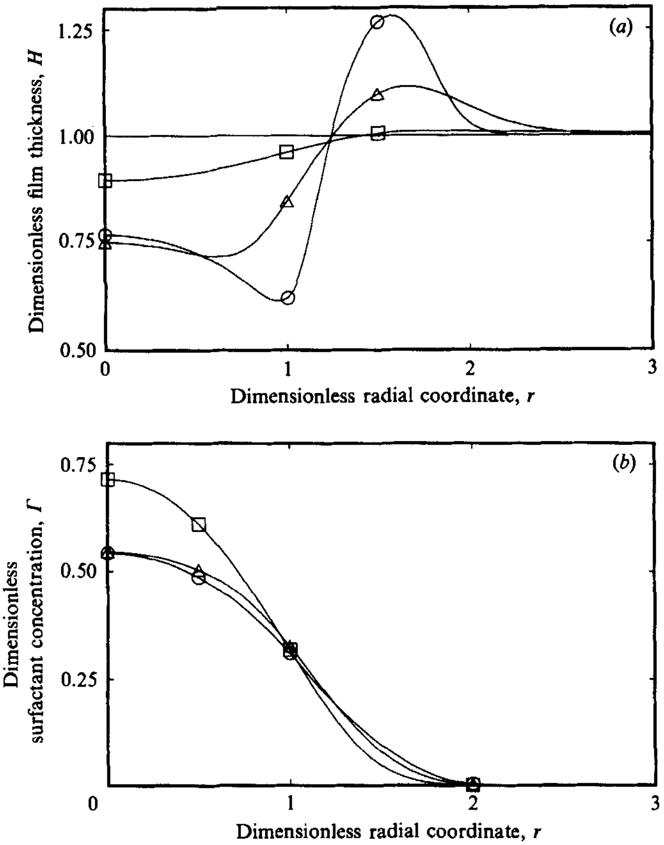

FIGURE 5. Film thickness and surfactant concentration profiles for ○, $G = 0.1$; △, $G = 1.0$; □, $G = 10.0$. $Pe = 10.0$, $\beta = 5.0$, $RI = 0.7$, $\Gamma_{\max} = 1.0$ and $t = 0.5$.

Figure 6(*a*) shows that the film responds to a decrease in β by increasing film disturbances near the leading edge and decreasing disturbances near the centre of the droplet. Figure 6(*b*) demonstrates that as β decreases more surfactant remains near the droplet centre.

The dependency of the film thickness and surfactant concentration profiles on the parameter RI is investigated by variation of RI with the total volume of surfactant, V_S, held constant

$$V_S = 2\pi \int_0^1 r\Gamma_{\text{init}}\,\mathrm{d}r = 2.29. \tag{4.1}$$

In this figure the values of RI are, $RI = 0$, 0.35 and 0.7. These initial concentration profiles are identical to those shown in figure 1. Figure 7(*a*) shows the film-thickness profiles at a fixed value of t. These profiles are remarkably similar near the leading edge, and the only major difference occurs in the central region of the droplet, where small values of RI lead to increased thinning. As RI decreases, the concentration of surfactant at the centreline increases, while only a minor modification of Γ is apparent near the leading edge.

Finally, we investigate the droplet radius as a function of time for different fixed values of Pe and G. The droplet radius, r_D, is calculated by the relationship

$$0.95V_S = 2\pi \int_0^{r_D} r\Gamma(r,t)\,\mathrm{d}r. \tag{4.2}$$

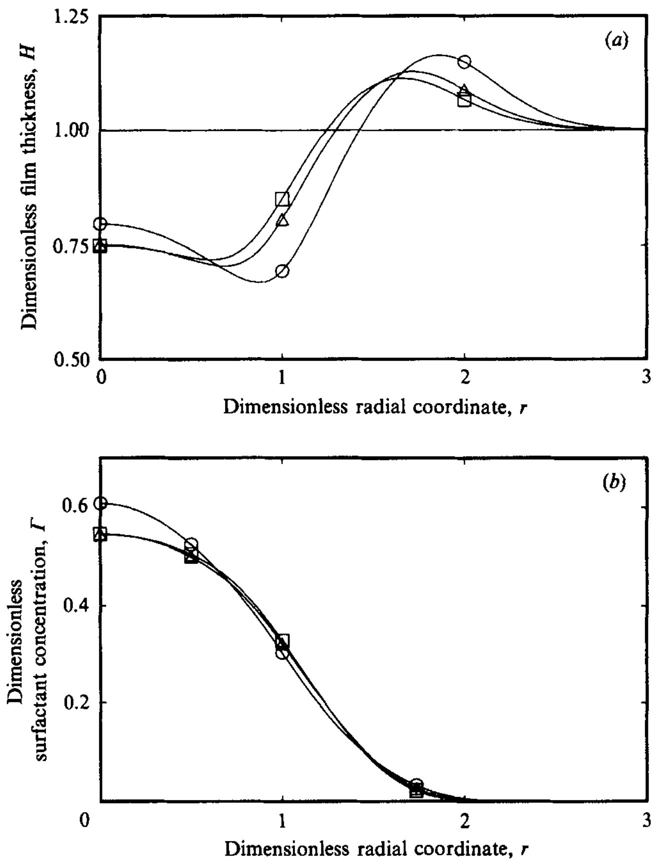

FIGURE 6. Film thickness and surfactant concentration profiles for ○, $\beta = 0.1$; △, $\beta = 1.0$; □, $\beta = 10.0$. $Pe = 10.0$, $G = 1.0$, $RI = 0.7$, $\Gamma_{\max} = 1.0$ and $t = 0.5$.

Figure 8 shows the droplet radius as a function of time for values of the $Pe = 1$, 10 and 100 with $G = 0$ and 1. This figure demonstrates increased spreading rates as Pe decreases. Additionally, as G increases for large Pe, the spreading rate decreases.

5. Large Péclet number spreading

As demonstrated by figure 4(*a*), when $Pe = 100$ the leading edge of the film-thickness profile is very steep and resembles a moving front. This behaviour may be understood by examining the limiting case of zero surface diffusivity and gravitational forcing ($G = 0, 1/Pe \rightarrow 0$). Equation (3.2) evaluated at $z = H$ shows that in this limit the radial velocity field is linear, with the maximum velocity at the surface,

$$v_r(r,H,t) = v_s(r,t) = \frac{\partial \sigma}{\partial \Gamma}\frac{\partial \Gamma}{\partial r}H. \tag{5.1}$$

In the limit of $1/Pe \rightarrow 0$, the surfactant is transported by convection only, so a well-demarcated concentration front may exist. Define the position of this front as $r = r_f$. Directly in front of the leading edge ($r = r_f^+$) no surfactant exists, so $\Gamma = \partial\Gamma/\partial r = 0$, and the magnitude of the radial surface velocity is $v_s(r_f^+, t) = v_s^+ = 0$. This leaves the undisturbed height $H^+ = 1$. Directly behind the concentration front ($r = r_f^-$)

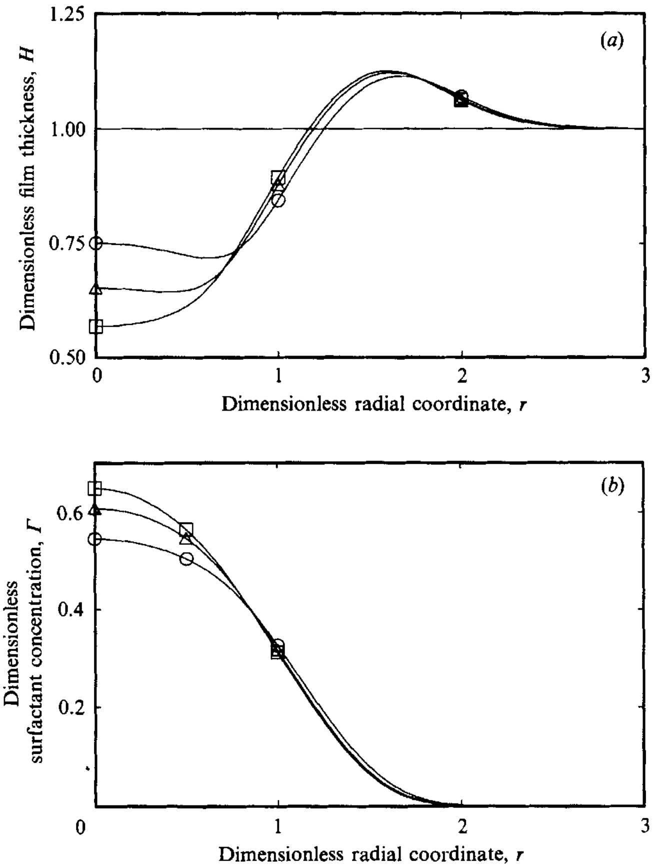

FIGURE 7. Film thickness and surfactant distribution profiles. ○, $RI = 0.7$; △, $RI = 0.35$; □, $RI = 0$ with $V_S = 2.29$. $Pe = 10.0$, $G = 1.0$, $\beta = 5.0$ and $t = 0.5$.

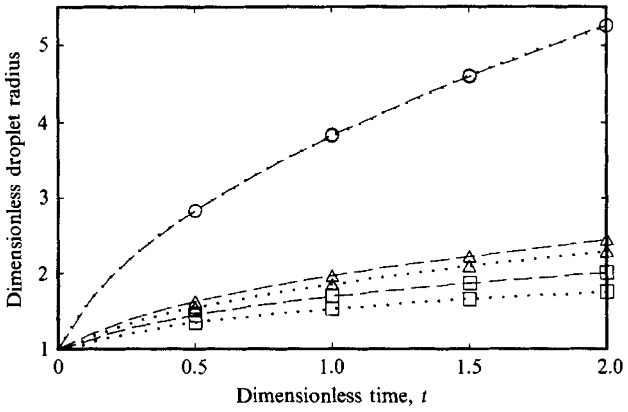

FIGURE 8. Droplet diameter, r_D, *vs*. time for ○, $Pe = 1.0$; △, $Pe = 10.0$; □, $Pe = 100$ with ----, $G = 0$; ....., $G = 1$. $\beta = 5.0$, $RI = 0.7$ and $\Gamma_{max} = 1.0$.

surfactant exists, so $\Gamma \neq 0$ and $\partial\Gamma/\partial r \neq 0$. The radial surface velocity there is $v_s(r_f^-, t) = v_s^-$. This shock discontinuity is characteristic of nonlinear kinematic waves (Whitham 1974). Accordingly, the shock speed is given in terms of the jump in volume flow rate divided by the jump in cross-sectional area of the film

$$\frac{\mathrm{d}r_f}{\mathrm{d}t} = \frac{2\pi r_f(\frac{1}{2}v_s^- H^- - \frac{1}{2}v_s^+ H^+)}{2\pi r_f(H^- - H^+)} = \frac{v_s^- H^-}{2(H^- - H^+)}. \tag{5.2}$$

Then, since the speed of the shock, $\mathrm{d}r_f/\mathrm{d}t$, must be equal to the surface speed, v_s^-, equation (5.2) shows that

$$H^- = 2. \tag{5.3}$$

This result is in agreement with the results of Borgas & Grotberg (1988) in their limit of zero diffusion. A consequence of the flow field is that the average thickness of the surfactant-covered film equals that of the undisturbed film, since the fluid ahead of the leading edge is not disturbed from its initially flat profile. Since the leading-edge film thickness is twice the undisturbed film thickness, the region behind the advancing front must have a magnitude less than that of the undisturbed film, which leads to the observed thinning region behind the leading edge. This result is in agreement with the leading-edge behaviour of our film-thickness profiles in the limit of large Pe and small G, figure 4 (*a*), where a moving front exists near the leading edge, and the slope of the surfactant concentration near $r = r_f$ is non-zero. In addition, this figure shows localized thinning occurring at a finite, non-zero, value of r. If the thinning is extreme, film rupture may occur. The solution found above for $Pe \rightarrow \infty$ is the 'outer' solution. To model the leading-edge 'inner' solution, the radial coordinate should be re-scaled as $\hat{r} = rPe^{\frac{1}{2}}$ in the evolution equations to preserve the highest-order spatial derivatives in (3.5). This shows that shock boundary layer has thickness of order $R_0/Pe^{\frac{1}{2}}$. If the modelling were to include the effects of capillarity, the region of infinite curvature should be rounded, modifying the shock structure.

6. Small Péclet number spreading

Here we investigate the spreading of a surface-active contaminant under conditions in which transport by surface diffusion dominates the transport due to surface-tension-gradient-induced convection. Two timescales exist in this problem, the diffusion timescale, T_D, and the convection timescale, T_C, defined as

$$T_C = \frac{\mu R_0^2}{SH_0}, \quad T_D = \frac{R_0^2}{D_s} = PeT_C. \tag{6.1}$$

Clearly, in the limit $Pe \rightarrow 0$, $T_C \gg T_D$, so most activity will occur on the diffusion timescale. We will thus approach this problem assuming that a boundary layer in time exists. The inner and outer dependent variables will be denoted $H^i(r, \tau)$, $\Gamma^i(r, \tau)$ and $H^o(r, t)$, $\Gamma^o(r, t)$, respectively, where the inner and outer timescales, τ and t, are based upon the diffusion and convection timescales respectively:

$$\tau = t^*/T_D, \quad t = t^*/T_C = Pe\tau. \tag{6.2}$$

6.1. *Inner solution*

The evolution equations ((3.4) and (3.5)), expressed in the inner variables are:

$$\frac{\partial H^{\mathrm{i}}}{\partial \tau}=\frac{Pe}{r}\frac{\partial}{\partial r}\left\{r\left[\frac{1}{3}\frac{\partial P}{\partial r}(H^{\mathrm{i}})^3-\tfrac{1}{2}(H^{\mathrm{i}})^2\sigma'(\Gamma^{\mathrm{i}})\frac{\partial \Gamma^{\mathrm{i}}}{\partial r}\right]\right\}, \tag{6.3}$$

$$\frac{\partial \Gamma^{\mathrm{i}}}{\partial \tau}=\frac{Pe}{r}\frac{\partial}{\partial r}\left\{r\left[\left(\frac{1}{Pe}-\Gamma^{\mathrm{i}}H^{\mathrm{i}}\sigma'(\Gamma^{\mathrm{i}})\right)\frac{\partial \Gamma^{\mathrm{i}}}{\partial r}+\frac{\partial P}{\partial r}\tfrac{1}{2}\Gamma^{\mathrm{i}}(H^{\mathrm{i}})^2\right]\right\}, \tag{6.4}$$

with $P(r,z,\tau)$ defined by (3.1). Assuming $Pe \leqslant 1$, we expand the dependent variables Γ^{i} and H^{i} in the regular expansions

$$H^{\mathrm{i}}(r,\tau)=H^{\mathrm{i}}_0(r,\tau)+PeH^{\mathrm{i}}_1(r,\tau)+O(Pe^2), \tag{6.5a}$$

$$\Gamma^{\mathrm{i}}(r,\tau)=\Gamma^{\mathrm{i}}_0(r,\tau)+Pe\Gamma^{\mathrm{i}}_1(r,\tau)+O(Pe^2). \tag{6.5b}$$

These series representations of H^{i} and Γ^{i} are substituted into the governing equations, and linear evolution equations are derived for each order in Pe. The $O(1)$ evolution equations are:

$$\frac{\partial H^{\mathrm{i}}_0}{\partial \tau}=0,\quad L_1\Gamma^{\mathrm{i}}_0=\left[\frac{\partial}{\partial r}-\frac{1}{r}\frac{\partial}{\partial r}\left[r\frac{\partial}{\partial r}\right]\right]\Gamma^{\mathrm{i}}_0=0. \tag{6.6a, b}$$

The solution of (6.6*a*) and initial condition (3.6*b*) is $H^{\mathrm{i}}_0(r,\tau)=1$, so the film retains its flat profile to $O(1)$. The solution of equation (6.6*b*) is found by solving the Green function problem,

$$L_1G(r,\tau;\eta,\hat{t})=\delta(r-\eta)\,\delta(\tau-\hat{t})/r, \tag{6.7}$$

where $G(r,\tau;\eta,\hat{t})$ is the Green function and δ is the Dirac delta function. The constraints on G are $G=0$ for $\tau<\hat{t}$, and $\lim_{r\to\infty}G=0$. $G(r,\tau;\eta,\hat{t})$ is found by Laplace transform to be:

$$G(r,\tau;\eta,\hat{t})=\frac{1}{2(\tau-\hat{t})}\exp\left\{\frac{-(\eta^2+r^2)}{4(\tau-\hat{t})}\right\}I_0\left\{\frac{r\eta}{2(\tau-\hat{t})}\right\}H(\tau-\hat{t}), \tag{6.8}$$

where I_0 is the modified Bessel function, and H is the Heaviside step function. The solution of (6.6*b*) is thus

$$\Gamma^{\mathrm{i}}_0(r,\tau)=\int_0^\infty \Gamma^{\mathrm{i}}_0(\eta,0)\,G(r,\tau;\eta,0)\,\eta\,\mathrm{d}\eta. \tag{6.9}$$

The $O(Pe)$ evolution equations are as follows:,

$$\frac{\partial H^{\mathrm{i}}_1}{\partial \tau}=\frac{1}{r}\frac{\partial}{\partial r}\left\{r\tfrac{1}{2}\sigma'(\Gamma^{\mathrm{i}}_0)\frac{\partial \Gamma^{\mathrm{i}}_1}{\partial \tau}\right\}=g_1(r,\tau), \tag{6.10a}$$

and

$$L_1\Gamma^{\mathrm{i}}_1=-\frac{1}{r}\frac{\partial}{\partial r}\left\{r\Gamma^{\mathrm{i}}_0\,\sigma'(\Gamma^{\mathrm{i}}_0)\frac{\partial \Gamma^{\mathrm{i}}_0}{\partial \tau}\right\}, \tag{6.10b}$$

where we have assumed that $\epsilon^2\beta=o(Pe)$ and $G=o(Pe)$ in order to delay the appearance of capillarity and gravity to next order. The $O(Pe)$ correction to the film thickness, $H^{i}_1(r,\tau)$, is found by integrating:

$$H^{\mathrm{i}}_1(r,\tau)=\int_0^\tau g_1(r,\hat{t})\,\mathrm{d}\hat{t}+H^{\mathrm{i}}_1(r,0), \tag{6.11}$$

where $g_1(r,\hat{t})$ is the right-hand side of equation (6.10*a*).

6.2. *Outer solution*

The outer solution is found from evolution equations (3.4) and (3.5) with the regular expansions of the outer dependent variables

$$H^{o}(r,t) = H^{o}_{0}(r,t)+PeH^{o}_{1}(r,t)+O(Pe^{2}), \tag{6.12a}$$

and

$$\Gamma^{o}(r,t) = \Gamma^{o}_{0}(r,t)+Pe\Gamma^{o}_{1}(r,t)+O(Pe^{2}). \tag{6.12b}$$

The $O(1)$ evolution equations for the outer variables are:

$$\frac{\partial H^{o}_{0}}{\partial t} = -\frac{1}{r}\frac{\partial}{\partial r}\left\{\frac{r(H^{o}_{0})^{2}}{2}\sigma'(\Gamma^{o}_{0})\frac{\partial \Gamma^{o}_{0}}{\partial r}\right\}, \quad \frac{1}{r}\frac{\partial}{\partial r}\left\{r\frac{\partial \Gamma^{o}_{0}}{\partial r}\right\} = 0. \tag{6.13a, b}$$

The solutions of equations (6.13*a*, *b*) with boundary conditions (3.7*a*–*d*) are $\Gamma^{o}_{0}(r, t) = 0$ and $H^{o}_{0}(r,t) = C_{0}(r)$. Matching the inner and outer $O(1)$ solution for film thickness, we find $C_{0}(r) = \lim_{\tau\to\infty} H^{i}_{0}(r,\tau) = 1$.

The $O(Pe)$ evolution equations are:

$$\frac{\partial H^{o}_{1}}{\partial t} = -\frac{1}{r}\frac{\partial}{\partial r}\left\{r\left[\tfrac{1}{2}\sigma'(\Gamma^{o}_{0})\frac{\partial \Gamma^{o}_{1}}{\partial r}\right]\right\}, \quad \frac{1}{r}\frac{\partial}{\partial r}\left\{r\left[\frac{\partial \Gamma_{1}}{\partial r}\right]\right\} = 0, \tag{6.14a, b}$$

whose solutions, after substitution of the boundary conditions (3.7*a*–*d*), are $\Gamma^{o}_{1}(r, t) = 0$ and $H^{o}_{1}(r,t) = C_{1}(r)$. Matching the inner and outer $O(1)$ solutions, we find

$$C_{1}(r) = \lim_{t\to 0} H^{o}_{1}(r,t) = \lim_{\tau\to\infty} H^{i}_{1}(r,\tau). \tag{6.15}$$

6.3. *Uniform expansion*

The uniform expansions, Γ_{0}, H_{0}, Γ_{1} and H_{1} are found by adding the inner and outer expansions, then subtracting their common part. These solutions are:

$$\Gamma_{0}(r,\tau) = \Gamma^{i}_{0}(r,\tau), \quad H_{0}(r,\tau) = H^{i}_{0}(r,\tau) = 1, \tag{6.16a, b}$$

$$\Gamma_{1}(r,\tau) = \Gamma^{i}_{1}(r,\tau), \quad H_{1}(r,\tau) = H^{i}_{1}(r,\tau). \tag{6.16c, d}$$

So, the uniform expansions are equal to the inner expansions, and all activity occurs on the diffusion timescale when $Pe \ll 1$.

Numerical solutions of $\Gamma_{0}(r,\tau)$ and $H_{1}(r,\tau)$, equations (6.9) and (6.11), were found using a Gauss–Konrad method for spatial integration and Runge–Kutta–Verner method for the temporal integration with initial conditions specified by equation (3.6*a*, *b*). Figure 9(*a*) compares H_{1} to the numerical solution of H from (3.4) and (3.5), plotted in the form $(H-1)/Pe$. The amplitude of the waveform H_{1} is larger than $(H-1)/Pe$, a difference that relates to the $O(Pe^{2})$ correction terms implicit in the $(H-1)/Pe$ form. Apparently, the $O(Pe^{2})$ interaction of diffusion with convection decreases the convective driving forces and leads to the smaller film disturbances. Likewise, figure 9(*b*) compares Γ_{0} with the numerical solution of Γ from (3.4) and (3.5). This figure demonstrates that convection (which enters at $O(Pe)$) increases the spreading rate, leading to a smaller surfactant concentration at $r = 0$.

Both figures 9(*a*) and 9(*b*) demonstrate that the solution of the small Péclet number analysis correlates well with the numerical solution to (3.4) and (3.5). In fact, the comparison with the profile representing $Pe = 1$ is remarkably good, since formally the perturbation method employed should not be successful when $Pe \approx O(1)$.

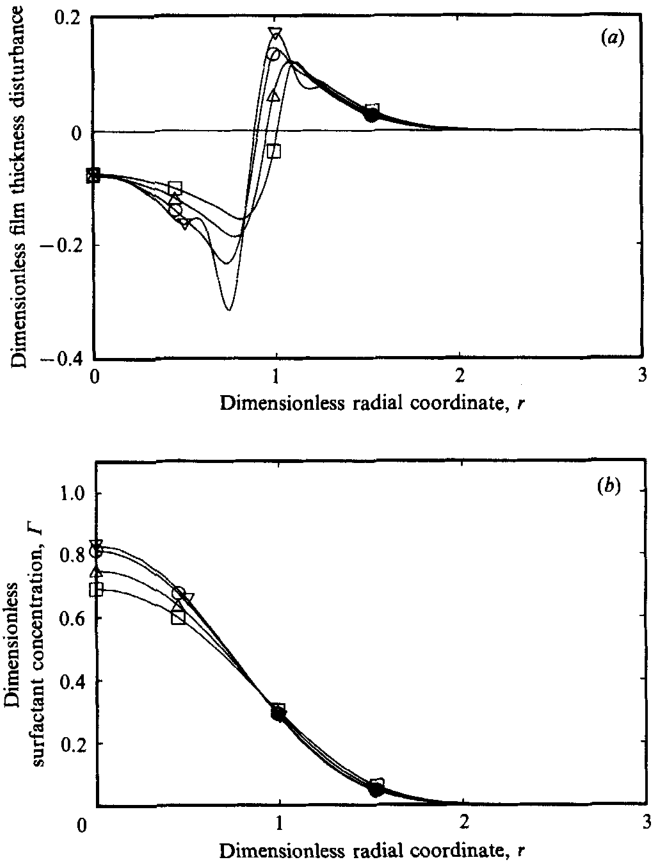

FIGURE 9. (*a*) Comparison of ▽, the $O(Pe)$ film disturbance profile, H_1, with $(H-1)/Pe$ found by numerical integration of equations (3.4) and (3.5). ○, $Pe = 0.1$; △, $Pe = 0.5$; □, $Pe = 1.0$. $G = 0$, $\beta = 5.0$, $\Gamma_{\max} = 1.0$, $RI = 0.7$ and $\tau = 0.1$. (*b*) Comparison of ▽, the $O(1)$ surfactant concentration profile, Γ_0, calculated using small Pe analysis, with Γ found by numerical integration of equations (3.4) and (3.5). ○, $Pe = 0.1$; △, $Pe = 0.5$; □, $Pe = 1.0$. $G = 0$, $\beta = 5.0$, $\Gamma_{\max} = 1.0$, $RI = 0.7$ and $\tau = 0.1$.

7. Discussion

The predicted behaviour of the surfactant/thin-film system may be understood by examining the interrelationships of the mechanisms included in our model. The mechanisms of surface diffusion and surface-tension gradients each arise from a non-uniform distribution of surfactant along the surface of the thin film. The diffusive process distributes the surfactant and decreases concentration gradients without disturbing the underlying film. In contrast, surface tension gradients are coupled to the thin film by the tangential-stress condition and thus drive convection within the thin film. Non-uniform convection leads to disturbances of the initially flat interface, which, in turn, influences the surfactant flow by modifying the viscous retardation. Finally, hydrostatic pressure gradients induce flows that restore the disturbed film to a uniform film thickness. The nonlinear coupling of these mechanisms leads to the behaviour observed in this study.

Figure 3 (*a*–*c*) describes the time-dependent Eulerian flow field. The flow is initially outward, as indicated by the streamlines in figure 3 (*a*). Near the juncture between

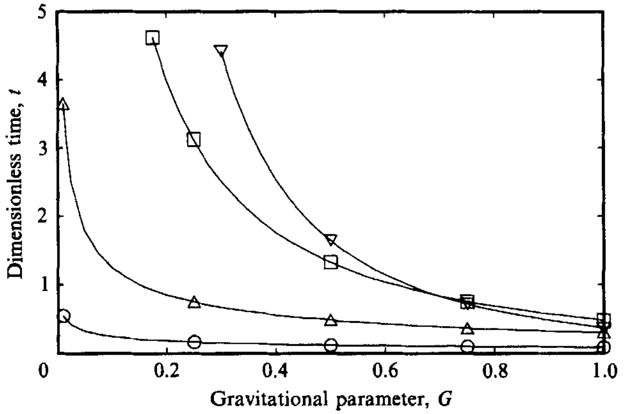

FIGURE 10. Flow-reversal onset time *vs.* G for ○, $Pe = 0.1$; △, $Pe = 1.0$; □, $Pe = 10.0$; ▽, $Pe = 100.0$. $\beta = 5.0$, $RI = 0.7$ and $\Gamma_{\max} = 1.0$.

the surfactant-covered and clean film, the fluid goes through a rapid transition from a large to a small radial velocity, since surface-tension gradients are small beyond this leading edge. This flow field leads to expulsion of fluid from regions of large surface-tension gradients, causing the film to thin. Fluid expelled from regions of large surface-tension gradients is retained near the surfactant's leading edge which leads to a build-up of fluid in that region. This behaviour is most evident in large Péclet number flows, as described in §5.

In regions where $\partial H/\partial r > 0$, the hydrostatic-pressure gradients and surface-tension gradients are in opposition. With time the hydrostatic forces increase, since film disturbances grow, and the surface-tension gradients diminish due to surfactant dilution and decreased concentration gradients. Eventually flow reversal results when the hydrostatic force overwhelms the surface-tension-gradient-induced flow near the bottom wall, which occurs when $GH\,\partial H/\partial r > (\partial\sigma/\partial\Gamma)(\partial\Gamma/\partial r)$. Streamlines describe the flow reversal in the form of a ring vortex, demonstrated by figure 3(*b*). As the surfactant continues to spread, the surface-tension-driven convection diminishes, and the backflow region grows so that the ring vortex engulfs the entire film behind the leading edge, as shown in figure 3(*c*). This flow pattern draws fluid from thick regions of the film and moves it to the thinner regions, causing a relaxation of disturbances towards a film of uniform thickness.

Figure 10 shows that for all values of Pe investigated, increasing G leads to an earlier flow reversal, since the gravitational forcing is enhanced. However, increasing Pe from 10 to 100 leads to a delay of flow reversal for $G < 0.75$, while for $G > 0.75$ the flow reversal occurs earlier. By increasing Pe (by decreasing D_s) the surfactant concentration gradients dissipate more slowly and $\partial H/\partial r$ becomes larger, which enhances hydrostatic-pressure gradients, as shown by figure 4(*a*, *b*). So, an increase in Pe leads to both an increase in the surface-tension and gravitational forcing. For $G < 0.75$, an increase of Pe from 10 to 100 enhances the surface-tension driving force to a greater degree than the gravitational driving force, so flow reversal is delayed. In contrast, increasing Pe from 10 to 100 when $G > 0.75$ increases gravitational forcing more than the surface-tension gradient forcing, leading to earlier flow reversal.

Figure 5(*b*) demonstrates that hydrostatic-pressure induced backflow decreases surfactant spreading rates. Modification of the flow field increases the viscous

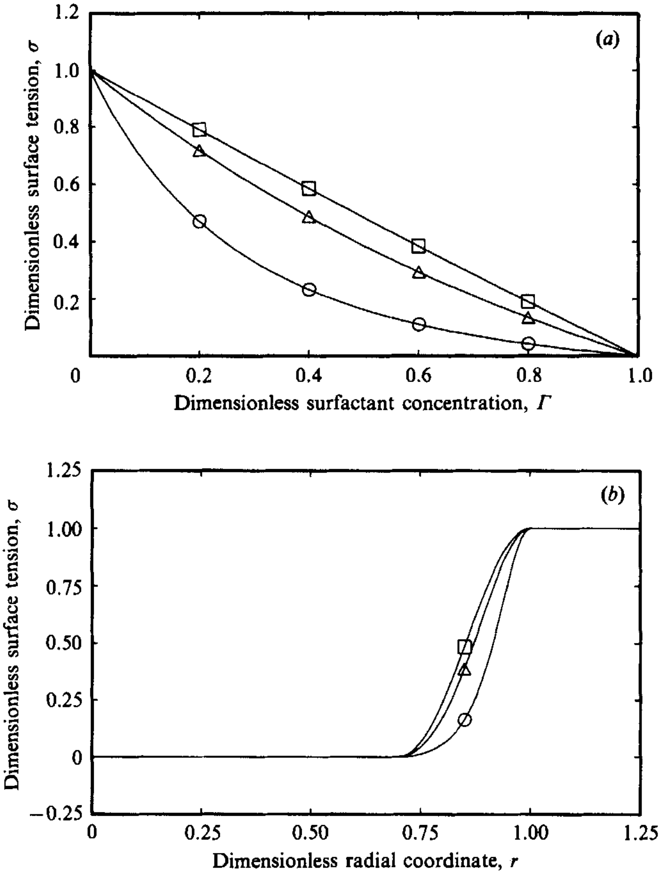

FIGURE 11. (*a*) Surface tension equation of state, equation (2.10). ○, $\beta = 0.1$; △, $\beta = 1.0$; □, $\beta = 10$. (*b*) Initial surface tension distribution, equation (3.6*a*). ○, $\beta = 0.1$; △, $\beta = 1.0$; □, $\beta = 10.0$. $RI = 0.7$ and $\Gamma_{max} = 1.0$.

retardation of the surface-film, and thus leads to a slowing of the convective transport of surfactant.

A small value of β implies that the surfactant is highly surface-active and also leads to a nonlinear equation of state, as shown by figure 11(*a*). When β is small, surface-tension gradients are a function of surface-concentration gradients and inversely related to the surface concentration. When β is large, the surface-tension gradients depend upon concentration gradients alone. This is shown in figure 11(*b*), the initial surface-tension distribution, which shows that as β decreases the magnitude of the surface-tension gradient decreases near the centre of the droplet, where concentrations are large, and increases near the edge of the droplet where concentrations are small.

It would be difficult to modify β while leaving all other parameters fixed. Nevertheless, such an experiment would demonstrate the influence of the nonlinear surface-tension equation of state (3.9*a*, *b*) on the spreading behaviour. Our predictions of such an experiment are shown in figure 6(*a*, *b*), where profiles are compared at constant t, which may correspond to different values of t^*. Owing to the mechanism listed above, small β increases disturbances near the edge of the droplet, where concentrations are small, and decreases disturbances near the centre, where

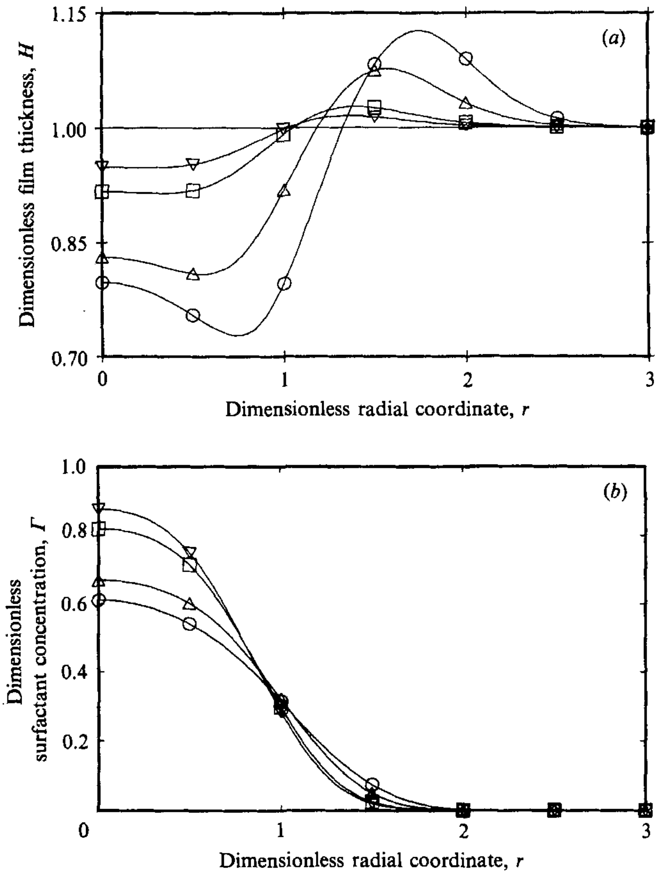

FIGURE 12. Film thickness and surfactant distribution profiles showing behaviour induced by modification of the surface activity, *S*. $\beta = (\sigma_0/S)-1$ = : ○, 0.25; △, 1.0; □, 5.0; ▽, 10.0. $Pe(\beta+1) = 60$, $G/(\beta+1) = 6.0$, $RI = 0.7$, $\Gamma_{max} = 1.0$ and $t(\beta+1) = 3.0$.

concentrations are large. Centreline concentrations increase as β decreases, since the inverse relationship of surface concentration to surface-tension gradients decreases the surfactant convection in that region. Droplet radius appears to be largely independent of β over the range of β investigated.

The effect of the parameter *RI* is demonstrated in figure 7(*a*, *b*). Essentially, *RI* locates the most important feature of the initial surfactant concentration profile – the position of the non-zero concentration gradient. As *RI* decreases, this gradient moves radially inward, inducing flows that create film deformations near the droplet centre. By increasing *RI*, the surface-tension gradients become localized near the leading edge. Since the imposed surface-tension difference must then occur over a smaller distance, the local concentration gradient increases, leading to larger convective forcing. The increase of *RI* is accompanied by localized film thinning at a finite, non-zero, radial position. If the thinning is extreme, the film may rupture, leading to the formation of a dry ring.

Figure 7(*b*) demonstrates that after a short time the surfactant distribution is largely independent of *RI*, especially near the leading edge. In fact, the leading-edge position is nearly identical for all cases investigated. Since *RI* is not easily defined in an experiment, this result is encouraging, as it shows that the predictions of droplet radius made by this model are fairly robust as a function of *RI*.

Figure 8 shows the droplet radius as a function of time for values of $Pe = 1$, 10 and 100 with $G = 0$ and 1. The spreading rate decreases with time in all cases, owing primarily to the dilution of the driving forces by convection and diffusion. As the Péclet number increases the spreading rate decreases, since the diffusive contribution is diminished as Pe increases, given our choice of timescale. Hydrostatic pressures modify the flow field and retard the distribution of surfactant, which is evident by the smaller droplet radius as G increases. The gravitational parameter does not strongly influence the small Pe results, where largely diffusive spreading occurs, as the film profile is not greatly disturbed and thus hydrostatic pressures remain small.

Practically, one would modify aerosol spreading behaviour by changing S, the surface-activity of the droplet. To investigate the influence of S we examine film and surfactant profiles with $\beta = \sigma_0/S - 1 = 0.25$, 1.0, 5.0 and 10.0 while fixing $Pe(\beta+1) = 60$, $G/(\beta+1) = 6.0$ and $t(\beta+1) = 3.0$. By setting the parameter magnitudes in this manner, the forcing is modified consistent with changes in S. Additionally, by fixing the non-dimensional time to the parameter β, the profiles may be interpreted as occurring at fixed t^*. When $\beta = 5.0$, the profiles represent our basic parameter set. Figure 12 demonstrates that a decrease in β increases film disturbances and the spreading rate. As β decreases, the surfactant becomes more surface-active, leading to an increase in convection which is characterized by an increase of Pe and a decrease of G. However, small β implies a nonlinear equation of state, which, on its own, would increase film disturbances near the leading edge and decrease disturbances near the droplet centre. Since this behaviour is not observed under the conditions of figure 12(*a*), the modification of the film is dominated by an overall increase of convective forcing, creating larger film disturbances and enhanced spreading rates.

8. Conclusions

We modelled an inhaled aerosol on the lung's liquid lining as a localized insoluble surfactant on a thin film, which is allowed to spread owing to surface-tension gradients and surface diffusion. Evolution equations describing the surfactant concentration and film thickness are derived, with solutions found numerically. The solutions demonstrate the relationships of surface-tension gradients, surface diffusion and gravity on the behaviour of a surfactant spreading on a thin viscous film. Analytical solutions found for cases of small and large Péclet numbers are in good agreement with our numerical results.

Previous investigators of spreading droplets have attempted to determine a simple relationship for the droplet radius as a function of time, typically expressed as $r_D = At^\alpha$. Ahmad & Hansen (1972) and Borgas & Grotberg (1988) predict a power-law relationship in which $\alpha = 0.5$. Simple experiments by Ahmad & Hansen (1972) and Joos & Pintens (1977) confirmed this relationship. To compare our results to those of the authors listed above, the local spreading rate, $k(t) = (t/r_D)\,dr_D/dt$, was determined by a central-difference method from the results plotted in figure 8. The power-law relationship is consistent with $k(t) = \alpha$. As can be seen from figure 13, $k(t)$ determined from this study is only marginally time-dependent. For convection-driven spreading ($Pe = 100$ and $G = 0$), the spreading droplet simulation provides values of $k(t) \approx 0.25$. When the value of the gravitational parameter G increases to $G = 1$, the spreading rate decreases to $k(t) \approx 0.20$. As the Péclet number decreases to

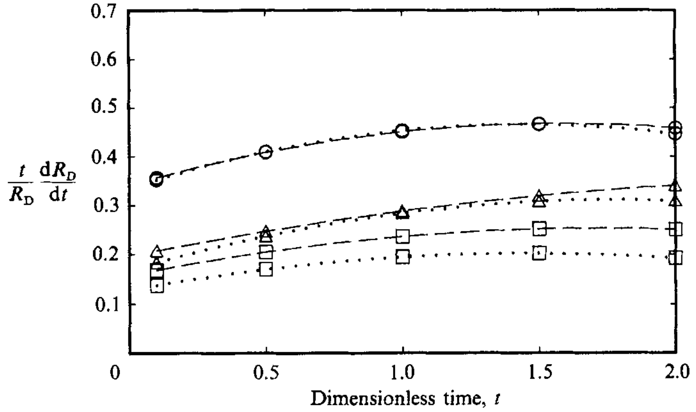

FIGURE 13. Spreading power, $k(t) = (t/R_D)\,(dR_D/dt)$, *vs.* time for ○, $Pe = 1.0$; △, $Pe = 10.0$; □, $Pe = 100$ with ----, $G = 0$; ....., $G = 1$. $\beta = 5.0$, $RI = 0.7$ and $\Gamma_{max} = 1.0$.

unity, the value of $k(t) \approx 0.5$, in agreement with the results of Ahmad & Hansen (1972), Joos & Pintens (1977) and Borgas & Grotberg (1988). However, only the analysis of Borgas & Grotberg (1988) includes surface diffusivity, and their predictions do not show a dependency of $k(t)$ on D_s. For this reason, it is fortuitous that their predictions of $k(t)$ compare to predictions based upon the spreading of a droplet in which convection and diffusion are of equivalent magnitude.

Several reasons might explain the poor correlation of the previous investigators' predictions with those of this study. Primarily, these analyses apply to a two-dimensional spreading planar front. The dilution of surfactant (and hence the forcing) is different in the case of a planar front from that of the axisymmetric spreading in cylindrical coordinates that we investigate. Also, their predictions rely on a quasi-steady analysis, while the behaviour is clearly time-dependent. Experimental measurements of surfactant spreading by Joos & Pintens (1977) and Ahmad & Hansen (1972) relied on surface marking the fluid with talc. This method may not be accurate due to the retarding effect of the talc as well as the talc's surface activity.

The intent of this study has been to develop an understanding of the mechanisms by which an inhaled aerosol may interact with the thin-film lining of the lung. We have seen from this theoretical analysis that a wide range of film behaviour is possible depending upon the magnitudes of the dimensionless parameters. Within the lung, the film lining has a range of thicknesses of 1–10 μm (Weibel 1963). With a film thickness of this magnitude, there will be essentially no effect due to gravity, since $G \ll O(1)$. When gravity fails to create a restoring force, other mechanisms such as capillarity may become important, so film relaxation is still possible. The form of this relaxation cannot be predicted from our analysis.

Depending upon the liquid-lining thickness, viscosity, surface tension and aerosol surface activity, inhaled aerosols may spread with characteristic Péclet numbers that are either small, large or $O(1)$. If Pe is much smaller than one, the aerosol will spread on the lung's liquid lining primarily by diffusion, and film disturbances will be small. If Pe is $O(1)$, an interaction of surface diffusion and convection will exist. In this regime, appreciable film disturbances will occur, and the relative magnitudes of diffusion and convection will influence the response of the thin film to the surfactant. Convection within the film could effect the transport of soluble substances from the droplet to the lung's parenchyma. For $Pe \gg O(1)$, large disturbances will be created and film rupture might occur, which may influence the lung's mechanical characteristics in the region of aerosol deposition.

We are appreciative of Dr Michael Borgas' contributions to this research, especially with §5. This research was funded by NIH grants K04-HL01818, R01-HL41126 and F32-HL07912 as well as NSF grant MSM-8351494 in conjunction with the General Motors Corporation and the Ryerson Foundation.

REFERENCES

ADLER, J. & SOWERBY, L. 1970 *J. Fluid Mech.* **42**, 549–559.

AHMAD, J. & HANSEN, R. S. 1972 *J. Colloid Interface Sci.* **38**, 601–604.

BORGAS, M. S. & GROTBERG, J. B. 1988 *J. Fluid Mech.* **193**, 151–170.

CONTE, J. E., HOLLANDER, H. & GOLDEN, J. A. 1987 *Ann. Intern. Med.* **107**, 495–498.

DAGAN, Z. 1984 *PhysicoChem. Hydrodyn.* **5**, 43–51.

DIPIETRO, N. D. & COX, R. G. 1980 *J. Fluid Mech.* **96**, 613–640.

DIPIETRO, N. D., HUH, C. & COX, R. G. 1978 *J. Fluid Mech.* **84**, 529–549.

ENHORNING, G., SHENNAN, A., POSSMAYER, F., DUNN, M., CHEN, C. P. & MILLIGAN, J. 1985 *Pediatrics* **76**, 145–153.

FODA, M. & COX, R. G. 1980 *J. Fluid Mech.* **101**, 33–51.

GOETZ, A. 1961 *Intl J. Air Water Poll.* **4**, 168–184.

HUSSAIN, Z., FATIMA, M. & AHMAD, J. 1975 *J. Colloid Interface Sci.* **50**, 44–48.

JOOS, P. & PINTENS, J. 1977 *J. Colloid Interface Sci.*, **60**, 507–513.

LEVICH, V. G. 1962 *Physicochemical Hydrodynamics.* Prentice Hall.

MERRITT, T. A., HALLMAN, M., BLOOM, B. T., BERRY, C., BENIRSCHKE, K., SAHN, D., KEY, T., EDWARDS, D., JARVENPAA, A., POHJAVUORI, M., KANKAANPAA, K., KUNNAS, M., PAATERO, H., RAPOLA, J. & JAASKELAINEN, J. 1986 *N. Engl. J. Med.* **315**, 785–790.

SCHRECK, R. M. 1982 *Air Pollution: Physiological Effects* (ed. J. J. McGrath & C. D. Barnes), ch. 7. Academic.

SHELUDKO, A. 1967 *Adv. Colloid Interface Sci.* **1**, 391–464.

WEIBEL, E. R. 1963 *Morphometry of the Human Lung.* Academic.

WHITHAM, G. B. 1974 *Linear and Nonlinear Waves.* John Wiley & Sons.

YIH, C.-S. 1968 *Phys. Fluids* **11**, 477–480.

YIH, C.-S. 1969 *Phys. Fluids* **12**, 1982–1987.

ZELTER, M., EXCUDIER, M. B. J., HOEFFEL, J. M. & MURRAY, J. F. 1988 In *Surfactant Replacement Therapy in Neonatal and Adult Respiratory Distress Syndrome* (ed. B. Lachmann), pp. 263–264. Springer.